Advanced Ultrasonic Imaging for Concrete: Alternative Imaging Conditions for Reverse Time Migration

Isabela COELHO LIMA, Maria GROHMANN, Ernst NIEDERLEITHINGER
BAM Bundesanstalt für Materialforschung und -prüfung, Berlin

Contact E-Mail: isabela.coelho-lima@bam.de

Abstract. Ultrasound echo is a widely used NDT technique for determining the internal geometry of structures. Reverse-time migration (RTM) has been recently introduced to NDT applications, as an imaging method for ultrasound data, to overcome some of the limitations (e.g. imaging steeply dipping reflector) experienced by the Synthetic Aperture Focusing Technique (SAFT), the most commonly used imaging algorithm for these measurements.

The standard implementation of RTM also experiences some drawbacks caused by its imaging condition, which is based on the zero-lag of the cross-correlation between source and receiver wavefields and generates high-amplitude low-frequency artifacts. Three alternative imaging conditions, developed for seismic data applications, were tested for their ability to provide better images than the standard cross-correlation: illumination compensation, deconvolution and wavefield decomposition. A polyamide specimen was chosen for the simulation of a synthetic experiment and for real data acquisition. The migrations of both synthetic and real data were performed with the software Madagascar. The illumination imaging condition was able to reduce the low-frequency noise and had a good performance in terms of computing time. The deconvolution improved the resolution in the synthetic tests, but did not showed such benefit for the real experiments. Finally, as for the wavefield decomposition, although it presented some advantages in terms of attenuating the low-frequency noise and some unwanted reflections, it was not able to image the internal structure of the polyamide as well as the cross-correlation did. Suggestions on how to improve the cost-effectiveness of the implementation of the deconvolution and wavefield decomposition were presented, as well as possible investigations that could be carried out in the future, in order to obtain better results with those two imaging conditions.

1. Introduction

The use of Non-Destructive Testing (NDT) methods in civil engineering is of fundamental importance to assure quality and safety during and after construction of structures. Ultrasonic techniques are frequently used to determine the location and shape of layers, voids and cracks within the overall background medium. Ultrasound systems used in NDT for civil engineering are generally of the pulse-echo type, i.e. based on wave reflection. In such systems, transducers acting as sources generate a high frequency (ultrasound) wave that propagates through the investigated body/object. Whenever this signal encounters a contrast

of acoustic impedance, part of it is reflected back towards the originating surface, where it can be recorded by receivers.

After acquisition, the data from pulse-echo systems need to go through a procedure called migration, so that the reflected signals are referenced to the correct position and an accurate image is generated. Typically, the imaging is done through Synthetic Aperture Focusing Techniques (SAFT), which implementation in time domain is closely related to the Kirchhoff migration, not only in its theory but also in its limitations [1], e.g. difficulty to image steep reflectors. The short-comings associated with this technique led to the use of other methods, such as Reverse Time Migration (RTM), which is able to image more complex structures. Despite the advantages over SAFT, RTM still has its drawbacks: it is computationally expensive and, on its standard implementation, the imaging condition is based on the zero-lag of the cross-correlation between the receiver and source wavefields, which may cause artifacts. Alternative imaging conditions have been presented by many authors, but they have not been explored in the context of NDT applications. The purpose of this work is, therefore, to test the applicability of the following alternative imaging conditions for RTM, in the scope of NDT for civil engineering: illumination compensation, deconvolution and wavefield decomposition. Within the next sections RTM will be briefly introduced, along with the definitions of the alternative imaging conditions, followed by the description and results of synthetic and real experiments over a polyamide specimen.

2. Reverse Time Migration

A method of growing interest in civil engineering, due its ability to image complex structures, is Reverse Time Migration (RTM). It is based on a time-marching wavefield reconstruction performed with a two-way (acoustic or elastic) wave equation, with numeric solutions implemented in the time domain [2]. Due to its ability to image steep reflectors and to account for multiples reflections as well as for multi-pathing, RTM is more accurate than SAFT.

In general, given a velocity model, the RTM for one shot point can be defined by three main steps:

- Forward time extrapolation of either measured or modeled source wavelet, into the velocity model, from the source location. Wavefield propagation can be simulated with a Finite Difference (FD) scheme.
- Reverse time extrapolation of the recorded data, back into the velocity model (also through FD), from the recording datum.
- Application of an imaging condition for every point in space.

The standard imaging condition consists in multiplying the two wavefields at each time step and summing all the products for a given point in space (i.e. taking the zero-lag of the cross-correlation of wavefields), so that at the end the high amplitudes correspond to a reflector position. For the 2D case, the zero-lag of the cross-correlation can be defined by the following expression:

$$I(z,x) = \sum_{s}\sum_{t} S_s(t,z,x)R_s(t,z,x) \qquad \text{(Eq. 1)}$$

where $S_s(t, z, x)$ and $R_s(t, z, x)$ are the source and receiver wavefields, and the subscripts *s* and *t* indicate the shot-point number and time, respectively (refer to Figure 1 for a general RTM scheme).

Although this imaging condition is quite robust and simple to implement, in the presence of strong impedance contrast and/or complex structures, the cross-correlation will generate low frequency, high amplitude artifacts (i.e. non-reflecting points will generate unwanted high cross-correlation results). To circumvent such drawback, alternative imaging

conditions have been proposed in literature, mainly to address issues faced by complex geology in the oil&gas industry. The aim of this work is to explore the advantages and applicability of different imaging conditions in the scope of NDT for civil engineering.

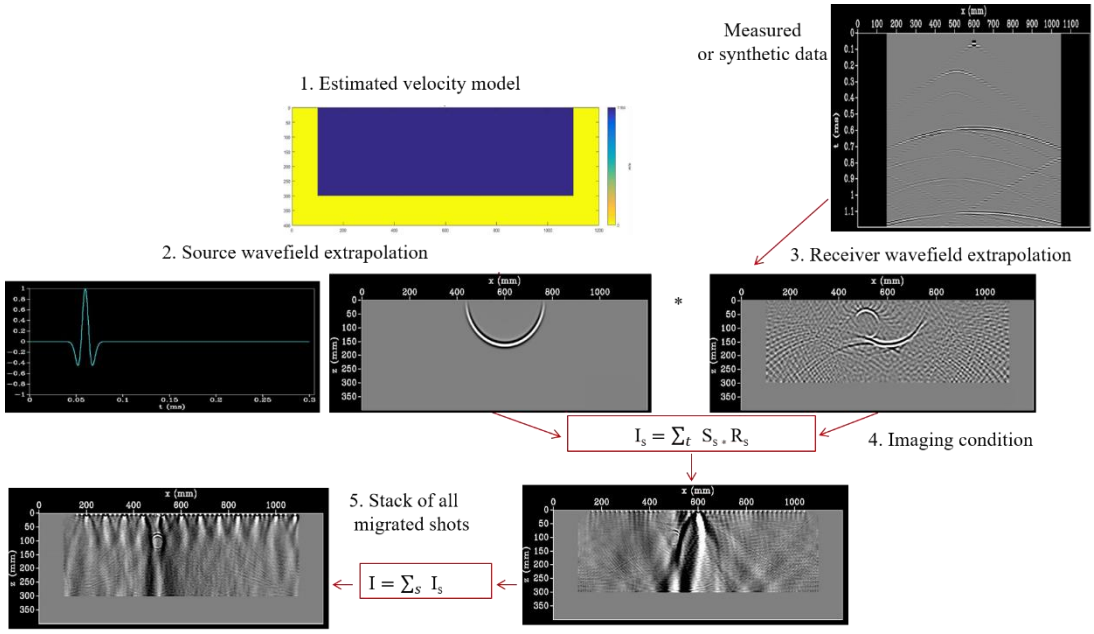

Figure 1RTM principle

2.1 Alternative Imaging Conditions

2.1.1 Illumination compensation

In [3] two alternative imaging conditions were introduced, using receiver and source illumination, to reduce/eliminate the low frequency artifacts caused by the conventional condition. The methods are based on the division, for each shot, of the cross-correlation, between source and receiver wavefields, by either the receiver illumination (Eq. 2) or the source illumination **Erro! Fonte de referência não encontrada.**, as stated below [3]:

$$I(z,x) = \sum_s \frac{\sum_t S_s(t,z,x) R_s(t,z,x)}{\sum_t R_s^2(t,z,x)} \qquad \text{(Eq. 2)}$$

$$I(z,x) = \sum_s \frac{\sum_t S_s(t,z,x) R_s(t,z,x)}{\sum_t S_s^2(t,z,x)} \qquad \text{(Eq. 3)}$$

Since the source and receiver illumination are derived from the correspondent wavefields (which are anyway computed for the conventional imaging condition), the proposed methods are simple to be implemented and do not require too much additional computation.

2.1.2 Deconvolution imaging condition

The second imaging condition tested defines the reflectivity strength as the zero lag deconvolution of the receiver wavefield, $R_s(x,z)$, by the source wavefield, $S_s(x,z)$, which can be generally stated as [4]:

$$\mathrm{I}(z,\mathrm{x}) = \frac{\mathrm{R_s}(z,\mathrm{x},\tau=0)}{\mathrm{S_s}(z,\mathrm{x},\tau=0)} \quad \text{(Eq. 4)}$$

where the division should be interpreted as deconvolution in time between the wavefields, for a lag τ=0. This imaging condition prevents the creation of artifacts originated by wavefield multi-pathing, which may occur if velocity anomalies are present. For this work, the deconvolution imaging condition was implemented in the frequency domain, by means of Fourier Transform, so that the reflectivity strength can be stated as:

$$\mathrm{I}(\mathrm{z},\mathrm{x}) = \sum_{\omega}^{\omega_{\mathrm{Nyq}}} \frac{\mathrm{R_s}(\omega)\mathrm{S_s^*}(\omega)}{\mathrm{S_s}(\omega)\mathrm{S_s^*}(\omega)+\epsilon^2} \quad \text{(Eq. 5)}$$

where ω_{Nyq} is the Nyquist frequency, the superscript (*) indicates the conjugate and ϵ is a stabilization constant, to avoid division by zero (several ways to define this constant are described in [5]).

2.1.3 Wavefield decomposition condition

The third imaging condition tested was based on the works of [6] and [7] and uses the decomposition of the source and receiver wavefields into their one-way components, which are then combined and correlated to form the image. The argument for such decomposition is that, if source and receiver wavefields reach a reflecting point/surface, they propagate in opposite directions with respect to the normal of the interface. Otherwise both wavefields will always propagate in the same direction along a wave path [6]. Since, for the conventional imaging condition, low-frequency artifacts appear when the cross-correlation between the two wavefields creates amplitudes at non-reflecting points, correlating only the components that propagate in opposite directions would assure the creation of images only at reflectors.

To demonstrate the implementation of the proposed imaging condition, [6] chose the scenario of a horizontal reflector (therefore with a vertical normal) for which the wavefields were decomposed into upgoing and downgoing. Mathematically, this partition can be defined as:

$$\mathrm{S}(\mathrm{t},\vec{\mathrm{x}}) = \mathrm{S_d}(\mathrm{t},\vec{\mathrm{x}}) + \mathrm{S_u}(\mathrm{t},\vec{\mathrm{x}}) \quad \text{(Eq. 6)}$$

And

$$R(\mathrm{t},\vec{\mathrm{x}}) = \mathrm{R_d}(\mathrm{t},\vec{\mathrm{x}}) + \mathrm{R_u}(\mathrm{t},\vec{\mathrm{x}}) \quad \text{(Eq. 7)}$$

where $\mathrm{S_u}$ and $\mathrm{R_u}$ are the source and receiver upgoing components, while $\mathrm{S_d}$ and $\mathrm{R_d}$ are the downgoing ones. Considering the integral form of the conventional cross-correlation imaging condition as:

$$\mathrm{I}(\vec{\mathrm{x}}) = \int_0^{\mathrm{T_{max}}} \mathrm{S}(\mathrm{t},\vec{\mathrm{x}})\mathrm{R}(\mathrm{t},\vec{\mathrm{x}})\mathrm{dt} \quad \text{(Eq. 8)}$$

and substituting (Eq. 6) and (Eq. 7) into it, the following expression is obtained:

$$\begin{aligned} I(\vec{x}) = &\int_0^{T_{max}} S_d(t,\vec{x})R_u(t,\vec{x})dt + \int_0^{T_{max}} S_u(t,\vec{x})R_d(t,\vec{x})dt \\ &+ \int_0^{T_{max}} S_u(t,\vec{x})R_u(t,\vec{x})dt + \int_0^{T_{max}} S_d(t,\vec{x})R_d(t,\vec{x})dt \\ &= I_{z1}(\vec{x}) + I_{z2}(\vec{x}) + I_{z3}(\vec{x}) + I_{z4}(\vec{x}) \end{aligned} \quad \text{(Eq. 9)}$$

where $I_{z1}(\vec{x})$ and $I_{z2}(\vec{x})$ are the cross-correlation of the source and receiver wavefield components traveling in opposite directions, while $I_{z3}(\vec{x})$ and $I_{z4}(\vec{x})$ are responsible for generating the low-frequency noise. Since the last 2 terms create unwanted events in the migration result, [6] proposes to exclude them. In [7] the term $S_u(t, \vec{x})$ $R_d(t,\vec{x})$ is also excluded, based on [8], where it was demonstrated that this part can generate a false image in RTM and, therefore, can be eliminated from the imaging condition. The final imaging condition implemented here can be stated as:

$$I(\vec{x}) = \int_0^{T_{max}} [S_d(t,\vec{x})R_u(t,\vec{x})]dt \qquad \text{(Eq. 10)}$$

As for the wave decomposition itself, since (Eq. 10) only needs the oppositely propagating components of the wavefields at each time, a numerically efficient strategy is to use only a 1D Fourier transform with respect to the z direction for the separation into up and downgoing components. Once the decomposition is performed, the decomposed wavefields are transformed back to the space-time domain and applied to (Eq. 10). Similarly, wave decomposition along the horizontal axis can be performed with a 1D Fourier transform with respect to the x variable.

3. Synthetic Experiments

3.1 Simulation model

In order to test the capabilities of the alternative imaging conditions, a velocity model simulating a real polyamide specimen was used. Other studies (e.g. [1], [9], [10]) have also adopted such model for their experiments, mainly to take advantage of the homogeneous, diffraction-free character of polyamide, and, therefore, avoid a model containing scattering points, as would be the case for heterogeneous multiphase materials like concrete.

The simulated specimen can be seen in Figure 2 and consists of a rectangular block of 1000 mm in the x direction and 300 mm in the z direction, containing a circular air inclusion of 50 mm diameter, centered at coordinates (x,z)=(500 mm, 100 mm). A 100 mm-thick air layer was added to the sides and to the bottom of the polyamide, while for the top part a free-surface condition was established. For this work, the synthetic tests as well as the real data acquisition were performed only with transverse waves (more specifically SH waves), therefore the velocity values of the polyamide area were set to 1150 m/s, whereas a value of 0 m/s was attributed to the air layer and to the air inclusion. The choice for SH waves was mainly motivated by the fact that there is no mode conversion of the incident wave into other modes for a 2D configuration. All simulations and migration tests of this work were made with the open source software Madagascar.

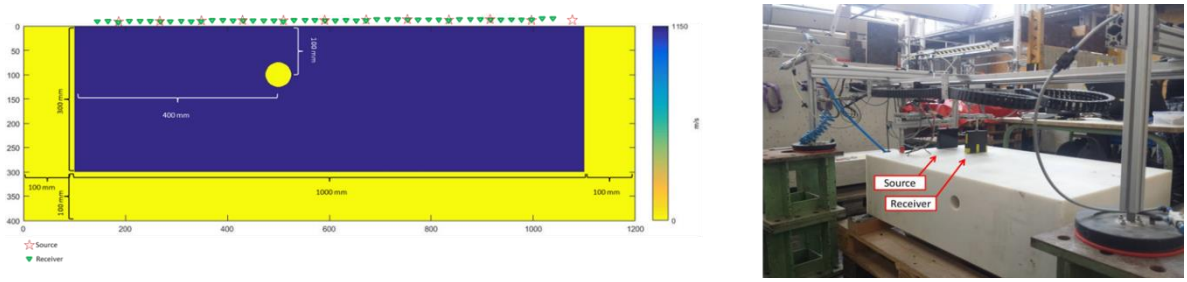

Figure 2 Real polyamide specimen (on the right) and its simulated version (on the left)

3.1.1 Simulation parameters

For the synthetic tests, a Ricker wavelet with center frequency of 50 kHz was used to model the source. The source wavelet was injected for 12 shot positions, spaced every 80 mm (illustrated by the red stars in Figure 2). The sampling in x and z were set to 1 mm, while the sampling in time was 0.0003 ms. For the generation of synthetic receiver data, the source wavelet was injected into the true velocity model, propagated through it via FD extrapolation, while the wavefield arriving at 45 receiver positions, spaced every 20 mm, was recorded (identified by green triangles in Figure 2). To assure that the data carries enough information for the imaging of the internal structures, a maximum recording time of 1.1997 ms was set.

3.2 Synthetic tests results

The migration results using the conventional and the alternative imaging conditions can be seen in Figure 3, where the arrows in red indicate artifacts that were either only present for that particular condition or that were reinforced by it.

The artifacts close to surface in the cross-correlation result were strongly attenuated by the illumination compensation. The edge artifacts in the bottom right corner of the cross-correlation image were mostly either eliminated or attenuated in the illumination compensation results. Although some unwanted events (e.g. reflection the from upper left corner as well as low frequency artifact, indicated by the red arrows) appeared for the receiver illumination, the image generated by it was very similar to the one originated with source illumination.

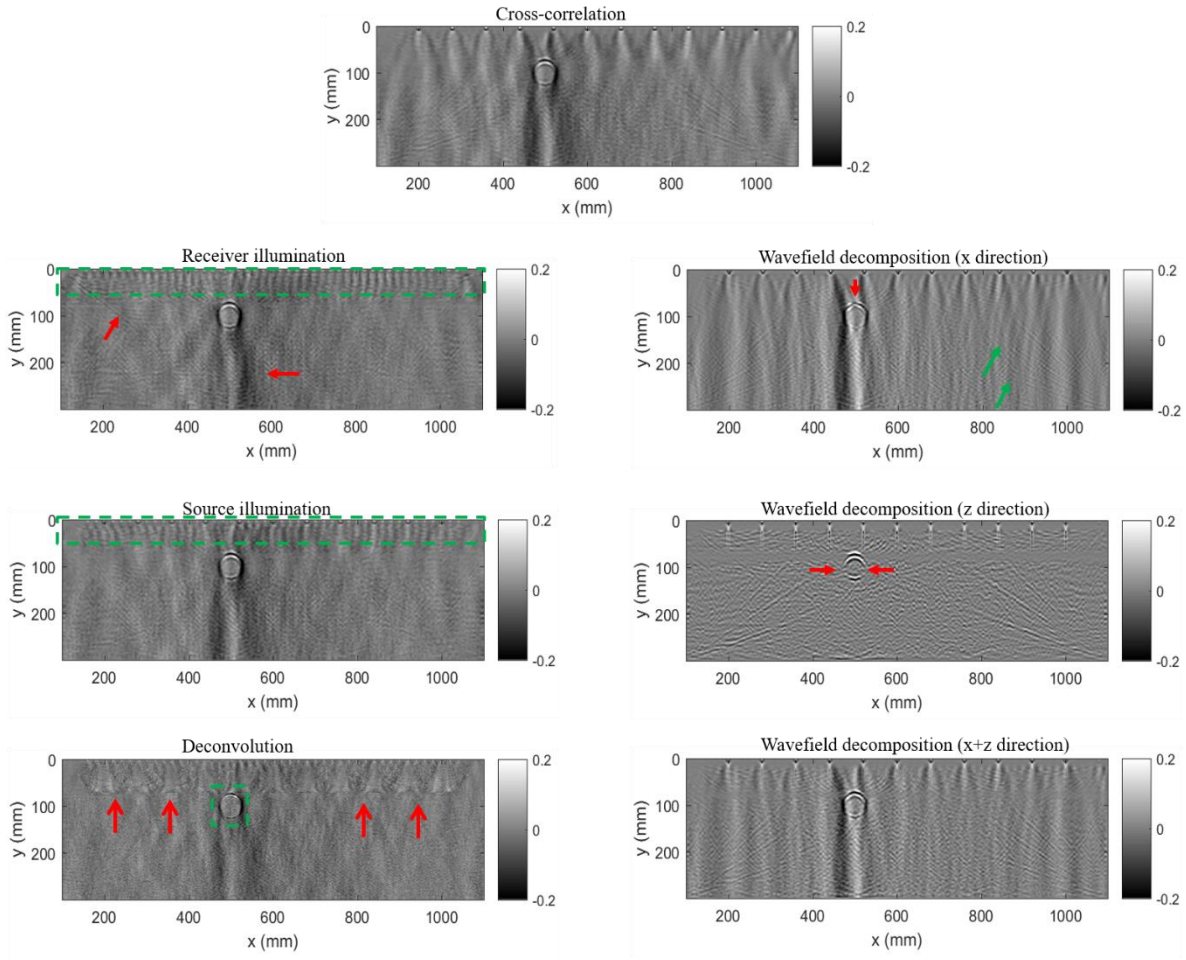

Figure 3 Synthetic tests results

Regarding the deconvolution results, it was able to remove some artifacts that were present in the cross-correlation, e.g. the ones close to the surface and the edge reflections. Most importantly, the air inclusion is much better resolved using this alternative condition, which consists in its most distinctive advantage when compared to the other methods. Nevertheless, some other noise was introduced, as indicated by the red arrows.

As for the wavefield decomposition, some artifacts from the Fourier Transform are present (close to the surface), for the decomposition in the z direction. In addition, it is possible to observe that the wavefield decomposition in z is only able to partially image the air inclusion. Regarding the decomposition in the x-direction, the inclusion was mostly imaged, although it presents a distortion in its circular shape, as indicate by the red arrow. It also has attenuated some of the reflections from the corners (green arrows). In order to take advantage of the imaging capacities of both decompositions, they were combined through an equal weight sum and the result can also be observed in Figure 3. Although the combined result defines the shape of the air inclusion better than the individual decompositions, no relevant benefit is observed in comparison to the cross-correlation results.

4. Real experiments

4.1 Measurement system

To conduct experiments over the real polyamide specimen, a scanner system, developed by BAM, was employed. The scanner is able to automatically generate and record ultrasound waves, which allows the data acquisition to be quite fast and accurate. The system consists of two moving axes (one where the source transducer is mounted and the other where the receiver transducer is mounted) which perform line measurements according to the specifications given by the operator (Figure 2).

4.2 Acquisition parameters

The first source position was located 24 mm away from the right edge of the specimen and the 11 subsequent shots moved towards the left direction, in 80 mm intervals. As for the receivers, a distance of 10 mm was set between them and a total of 94 positions were defined. The maximum offset in this setup was of 916 mm. Just as for the synthetic tests, the main source frequency was set to 50 kHz.

4.3 Pre-processing

Before performing migration on the real data, some pre-processing steps were needed, not only to ensure a stable wavefield extrapolation for RTM, but also to improve the quality of the recorded data. The following processes were applied to the raw data:

- Band-pass filter with lower and upper frequency limits of 8 kHz and 150 kHz, respectively.
- Interpolation in time to a finer sampling of 0.0001 ms, to ensure the stability of the finite difference scheme.
- 3D/2D correction, where first an amplitude correction is performed by multiplying the data with $\sqrt{t}$, then the result is convolved with $\frac{1}{\sqrt{t}}$ to correct for any phase mismatch [11]. As a consequence of the 3D nature of the investigated polyamide specimen, using a 2D migration may not generate

accurate images due to off-plane 3D effects. Therefore this correction is needed to compensate for such inaccuracies.

4.4. Post-processing

For the comparison of the migrated results, only shot points 2 to 6 were used for the stack. This combination was adopted after verifying that some shots points were introducing a strong amplitude artifact on top of the air inclusion, resulting in a poor image.

The stacks also went through a 2D high-pass Gaussian filter [12], which was implement by first applying a low-pass Gaussian filter (of kernel size 40 and standard deviation 10) and then subtracting the result from the unfiltered image.

4.5 Real experiment results

The migration results for the real data, using the conventional and the alternative imaging conditions, can be seen in Figure 4. The shapes in green indicate the areas where the tested condition generates a better image when compared to the conventional one.

The green rectangle in the receiver illumination condition shows the area where part of the low-frequency artifact was attenuated. The green arrow indicates a zone of image enhancement, where the continuity of the air inclusion was improved. On the other hand, one can notice that the low frequency noise is not completely removed and some events, e.g. reflections from the edges (red arrow), are reinforced. Similar to the receiver condition, the source illumination compensation was also able to attenuate some of the low-frequency artifacts (green rectangle). Nevertheless, the same drawback of enhancing some unwanted events was observed.

Regarding the deconvolution tests, unlike the synthetic results, no obvious improvement in the resolution is observed. Apart from the slight attenuation of the artifacts close to the source, no clear improvement is noticed.

As for the wavefield decomposition condition in the x-direction, it did not image the air inclusion as well as the cross-correlation, but was able to attenuate some reflections from the corners, particularly from the upper right one (green triangle). The decomposition in the z-direction managed to remove great part of the low-frequency noise of the conventional condition, especially near the surface (green rectangle). On the other hand, the sides of the air inclusion were poorly imaged and the bottom had a flatter shape. Although the combination of the individual decompositions produced an image of the air inclusion very similar to the cross-correlation one, it also "brought back" the low-frequency artifacts and corner reflections.

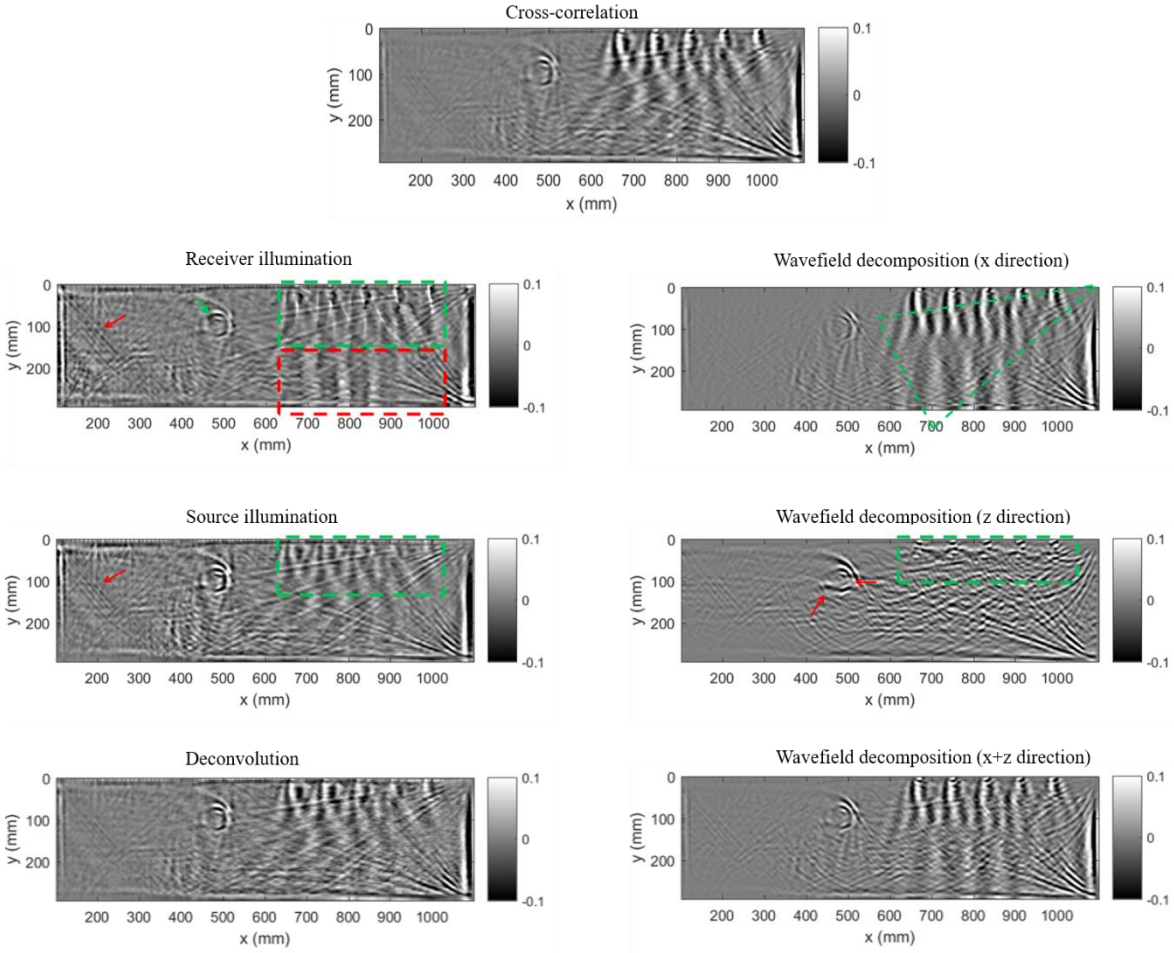

Figure 4 Real experiments results

5. Conclusion

Synthetic tests as well as experiments over a real polyamide specimen were conducted to analyze if imaging conditions, alternative to the conventional cross-correlation, could bring benefits to RTM results of ultrasound data, in the context of NDT applications. The three conditions tested were illumination compensation, deconvolution and wavefield decomposition. Both synthetic and real data experiments showed benefits in reducing the low-frequency artifacts by using the illumination compensation, which makes these conditions relevant for future studies, especially considering the low-extra cost in terms of computing time. As for the deconvolution imaging condition, it improved the resolution when applied to synthetic data although the same effect was not observed for the real experiments. Further developments to automatically define the optimal value for ϵ and to improve the algorithm's efficiency, could lead to improved performance and imaging for this condition. Finally, the tests with wavefield decomposition in the x and z directions provided some improvements when compared to the cross-correlation (e.g. attenuation of reflections from the corners and of low-frequency artifacts, respectively), but did not resulted in better imaging of the air inclusion. Further investigation on the implementation of this condition should be carried in order to validate the results.

References

[1] S. Müller, E. Niederleithinger, and T. Bohlen, “Reverse Time Migration: A Seismic

Imaging Technique Applied to Synthetic Ultrasonic Data," *Int. J. Geophys.*, vol. 2012, Arti, 2012.

[2] P. Sava and S. J. Hill, "Overview and classification of wavefield seismic imaging methods," *Lead. Edge*, vol. 28(2), pp. 170–183, 2009.

[3] B. Kaelin and A. Guitton, "Imaging condition for reverse time migration," in *SEG/New Orleans 2006 Annual Meeting*, 2006.

[4] A. A. Valenciano and B. Biondi, "Deconvolution imaging condition for reverse-time migration," *Stanford Explor. Proj.*, vol. Report 112, pp. 83–96, 2002.

[5] J. Schleicher, J. C. Costa, and A. Novais, "A Comparison of Imaging Conditions for Wave-Equation Shot-Profile Migration," in *4o PDPETRO, Campinas, SP*, 2007.

[6] F. Liu, G. Zhang, S. A. Morton, and J. P. Leveille, "An effective imaging condition for reverse-time migration using wavefield decomposition," *Geophysics*, vol. Vol. 76, N, pp. S29–S39, 2011.

[7] Y. Wang, Y. Zheng, Q. Xue, X. Chang, T. W. Fei, and Y. Luo, "Reverse time migration of multiples: Reducing migration artifacts using the wavefield decomposition imaging condition," *Geophys. Vol. 82, NO. 4 (July-August 2017); P. S307–S314*, 2017.

[8] T. W. Fei, Y. Luo, J. Yang, H. Liu, and F. Qin, "Removing false images in reverse time migration:The concept of de-primary," *Geophys. Vol. 80, NO. 6 (November-December 2015); P. S237–S244*, 2015.

[9] S. Müller and E. Niederleithinger, "Anwendung der Reverse Time Migration auf Ultraschall-Echo-Messungen in der zerstörungsfreien Prüfung im Bauwesen," *DGZfP-Jahrestagung 2014 – Di.1.C.4*, 2014.

[10] M. Grohmann, S. Müller, and E. Niederleithinger, "Reverse Time Migration: Introduction of a New Imaging Technique for Ultrasonic Measurements in Civil Engineering," *Int. Symp. Non-Destructive Test. Civ. Eng.*, 2015.

[11] E. Crase, A. Pica, M. Noble, J. McDonald, and A. Tarantola, "Robust elastic nonlinear waveform inversion: Application to real data," *Geophys. 55(5)527–538*, 1990.

[12] R. C. Gonzalez and R. E. Woods, *Digital image processing*. Pearson/Prentice Hall, 2008.